

Effect of Electrical Contact Resistance on Performance and Transport Characteristics of Proton Exchange Membrane Fuel Cells

Shian Li¹, Rongqiang Wei¹, Yuanxin Qi², Guogang Yang^{1,*}, Qiuwan Shen^{1,*}

¹ Marine Engineering College, Dalian Maritime University, Dalian, China;

² Department of Energy Sciences, Lund University, Lund, Sweden;

*E-mail: yanggg@dlnu.edu.cn and shenqiuwan@dlnu.edu.cn

Received: 2 August 2019 / Accepted: 25 September 2019 / Published: 29 October 2019

In this study, the effect of electrical contact resistance on cell performance and local transport characteristics of proton exchange membrane fuel cells (PEMFCs) are numerically investigated by using a two-dimensional, non-isothermal and two-phase flow fuel cell model. The conservation equations of species, temperature, charge, liquid water and dissolved water were solved to investigate the transport processes of heat and mass transfer, electron and proton transports, liquid water formation and transport, and water transport through the membrane. The mathematical model was validated against the experimental data reported in the open literature. Results showed that the performance is significantly affected by the electrical contact resistance, especially at low cell voltages. In addition, the temperature, liquid water saturation and solid phase potential distribution profiles are greatly influenced by the existence of electrical contact resistance.

Keywords: PEMFCs, Modeling, Contact resistance, Cell performance, Transport phenomena

1. INTRODUCTION

Fuel cells are energy conversion devices where the chemical energy of a fuel is directly converted to electrical and thermal energy [1-4]. Proton exchange membrane fuel cells (PEMFCs) can be used as alternative power sources for different applications [5-7]. PEMFCs consist of several components: the current collectors, the gas diffusion layers (GDLs), the catalyst layers (CLs) and the membrane. The hydrogen oxidation reaction (HOR) and oxygen reduction reaction (ORR) take place simultaneously in the CLs to produce electricity.

The cell performance and lifetime of PEMFCs can be significantly affected by temperature. The effect of thermal boundary condition (constant temperature and insulated boundary conditions) on

temperature distributions within PEMFCs were investigated by Shimpalee and Dutta [8]. It was found that the overall performance and local transport phenomena of PEMFCs were significantly affected by the thermal boundary conditions applied. A two-phase and non-isothermal model was developed to examine the liquid water distribution and flooding issues [9]. The temperature distributions inside fuel cells are also influenced by the design of cooling plates [10-11]. The cell performance of PEMFCs is also affected by the electron transport. A three-dimensional, single-phase, isothermal numerical model was adopted to study the effect of electron transport through the GDL. Results showed that the magnitude and distribution of current density were significantly affected by the electrical conductivity of the GDL [12]. A three-dimensional, single-phase, non-isothermal model was used to study the performance of PEMFCs with electrical contact resistance [13]. And a parametric study was also carried out to investigate the effect of flow channel dimensions on the fuel cell performance.

Experimental measurements have already been carried out to investigate the electrical contact resistance between the current collector and GDL [14-16]. It was found that the electrical contact resistance is quickly decreased and then reaches a constant value when the assembly force is gradually increased. Although there are many studies related to the performance and transport characteristics within PEMFCs, a comprehensive study taking into account the electrical contact resistance is still very few. The performance of PEMFCs with electrical contact resistance has already been studied in ref.[13], but the effect of liquid water was not considered. In this study, a two-dimensional, non-isothermal and two-phase flow model was employed to investigate the cell performance and local transport phenomena of PEMFCs with/without the electrical contact resistance.

2. MODEL DESCRIPTION

2.1 Physical model and assumptions

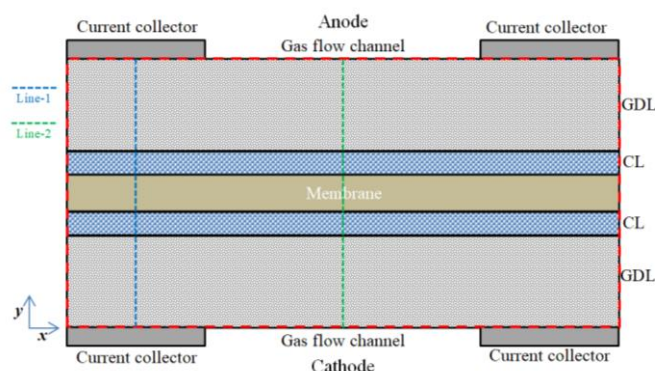


Figure 1. Schematic of proton exchange membrane fuel cells.

In this study, a two-dimensional mathematical model including the electrical contact resistance was developed for the PEMFCs. As shown in fig. 1, the computational domain consists of several layers, i.e., the GDLs, CLs and the membrane between the anode and cathode electrodes. Line-1 is located in the middle of current collector regions, and Line-2 is placed in the gas flow channel regions.

The geometric parameters and the operating conditions are presented in Table 1. In the fuel cell mathematical model, ideal gas law is applied for the reactant gases; the CLs are homogeneous and isotropic; the reactant gases cannot diffuse across the membrane; the generated water in the cathode CL is in dissolved phase [7, 17].

2.2 Governing equations

Species conservation equation:

$$\nabla \cdot (\rho \vec{u} Y_i) = \nabla \cdot (\rho D_{eff,i} \nabla Y_i) + S_i \quad (1)$$

where Y_i is the mass fraction and $D_{eff,i}$ is effective diffusivity for the i th species. S_i is the source term.

Energy conservation equation:

$$\nabla \cdot (\rho c_p \vec{u} T) = \nabla \cdot (k_{eff} \nabla T) + S_T \quad (2)$$

where c_p is the specific heat and k_{eff} is the effective thermal conductivity. The irreversible, reversible and ohmic heat generation are included in the source term.

Charge conservation equation:

$$\nabla \cdot (\sigma_{eff,s} \nabla \phi_s) + S_s = 0 \quad (3)$$

$$\nabla \cdot (\sigma_{eff,m} \nabla \phi_m) + S_m = 0 \quad (4)$$

where $\sigma_{eff,s}$ and $\sigma_{eff,m}$ are the effective electrical conductivity and protonic conductivity, respectively. ϕ_s is the electrical potential, and ϕ_m is the protonic potential. The Butler-Volmer equation and spherical agglomerate model are employed to describe the HOR and ORR in the CLs, respectively.

Liquid water transport equation:

$$\nabla \cdot \left(\rho_l \frac{K_{rl} \mu_g}{K_{rg} \mu_l} \vec{u} \right) = \nabla \cdot (\rho_l D_s \nabla S) + S_l \quad (5)$$

where K_{rl} is the relative permeability of liquid phase and K_{rg} is the relative permeability of gas phase. D_s is the capillary diffusion coefficient. S_l is the source term.

Dissolved water transport equation:

$$-\nabla \cdot \left(\frac{n_d}{F} \sigma_m \nabla \phi_m \right) = \nabla \cdot \left(\frac{\rho_m}{M_m} D_\lambda \nabla \lambda \right) + S_d \quad (6)$$

where n_d and D_λ are the electro-osmotic drag coefficient and water diffusivity in the membrane, respectively. S_d is the corresponding source term.

The corresponding expressions, parameters and source terms mentioned above are summarized in Tables 2-4. More detailed information can be found in [17].

2.3 Numerical implementation and boundary conditions

The fuel cell model is implemented using the commercial software ANSYS FLUENT. The user defined functions (UDFs) are used to define the transport equations, source terms and the parameters in the mathematical model.

At the gas flow channel and GDL interface, the species mass fractions are prescribed. In addition, the liquid water saturation is assigned as zero. The operating temperature and a constant electric potential, $\phi_s=0$, are specified at the anode current collector and GDL interface. At the cathode terminal, the operating temperature and a constant electric potential, $\phi_s=V_{\text{cell}}$, are applied at the cathode current collector and GDL interface. And the detailed boundary conditions are found in ref. [18]. The electrical contact resistance is applied at the anode/cathode current collector and GDL interface, the detailed information of the implementation of contact resistances can be found in ref. [19]. In this study, the operating temperature is 353 K, and the operating pressure is 1.0 atm. It is assumed that hydrogen and air are fully humidified. And then the corresponding mass fraction is calculated.

Table 1. Fuel cell geometric parameters and operating conditions [14].

Parameter	Value	Unit
Fuel cell width	2	mm
Gas flow channel width	1	mm
Anode/Cathode GDL thickness	0.2	mm
Anode/Cathode CL thickness	0.01	mm
Membrane thickness	0.05	mm
Operating pressure, P_a/P_c	1.0	atm
Operating temperature, T_a/T_c	353	K

Table 2. Complementary expressions [14].

Parameter	Value	Units
Platinum loading, m_{pt}	0.4	mg cm ⁻²
Platinum density, ρ_{pt}	2.145×10^4	kg m ⁻³
Carbon loading, m_c	0.6	mg cm ⁻²
Carbon density, ρ_c	1.8×10^3	kg m ⁻³
Dry membrane density, ρ_m	1.98×10^3	kg m ⁻³
Membrane equivalent weight, M_m	1.1	kg mol ⁻¹
Porosity of GDL, ϵ_{GDL}	0.6	-
Anode reference exchange current density, i_a^{ref}	100	A m ⁻²
Cathode reference exchange current density, i_c^{ref}	$10^{(0.03741 * T - 16.96)}$	A m ⁻²
Anode transfer coefficient, α_a	0.5	-
Cathode transfer coefficient, α_c	1	-
Reference hydrogen concentration, $c_{H_2}^{ref}$	56.4	mol m ⁻³
Reference oxygen concentration, $c_{O_2}^{ref}$	3.39	mol m ⁻³
Hydrogen Henry's constant, H_{H_2}	4.56×10^3	Pa m ³ mol ⁻¹
Oxygen Henry's constant, H_{O_2}	$0.101325e^{(-666/T+14.1)}$	Pa m ³ mol ⁻¹
Thermal conductivity of GDL/CL, $k_{GDL/CL}$	1.7/0.3	W m ⁻¹ K ⁻¹
Thermal conductivity of membrane, k_m	0.25	W m ⁻¹ K ⁻¹
Electrical conductivity of GDL/CL, $\sigma_{s,GDL/CL}$	5000/2000	S m ⁻¹
Entropy of hydrogen oxidation, ΔS_a	0.104	J mol ⁻¹ K ⁻¹

Entropy of oxygen reduction, ΔS_c	-326.36	$\text{J mol}^{-1} \text{K}^{-1}$
Latent heat of condensation/evaporation, Δh_{lg}	2.36×10^6	J kg^{-1}
Liquid water viscosity, μ	3.517×10^{-4}	Pa s
Surface tension, σ	0.0625	N m^{-1}
Contact angle of GDL/CL, $\theta_{GDL/CL}$	$110^\circ/95^\circ$	-
Condensation rate, γ_{con}	100	s^{-1}
Evaporation rate, γ_{evap}	100	s^{-1}
Dissolved water phase change rate, γ	1	s^{-1}
Permeability of GDL, K_{GDL}	5.6×10^{-12}	m^2
Permeability of CL, K_{CL}	1.0×10^{-13}	m^2
Binary diffusivity, $D_{H_2-H_2O}$	9.15×10^{-5}	$\text{m}^2 \text{s}^{-1}$
Binary diffusivity, $D_{O_2-H_2O}$	2.82×10^{-5}	$\text{m}^2 \text{s}^{-1}$
Binary diffusivity, $D_{O_2-N_2}$	2.2×10^{-5}	$\text{m}^2 \text{s}^{-1}$
Binary diffusivity, $D_{H_2O-N_2}$	2.56×10^{-5}	$\text{m}^2 \text{s}^{-1}$

Table 3. Complementary equations and definitions [14].

Description		Units
Effective mass diffusivity	$D_{eff,i} = (1 - s)^{1.5} \epsilon^{1.5} D_{i,m}$	$\text{m}^2 \text{s}^{-1}$
Mass diffusivity	$D_{i,m} = \frac{1 - X_i}{\sum_{j=1, j \neq i}^n X_j / D_{i,j}}$	$\text{m}^2 \text{s}^{-1}$
Binary mass diffusivity	$D_{i,j} = D_{i,j}(T_0, P_0) \left(\frac{P_0}{P}\right) \left(\frac{T}{T_0}\right)^{1.5}$	$\text{m}^2 \text{s}^{-1}$
Electrochemical kinetics	$j_a = (1 - s) i_a^{ref} a_{eff} \left(\frac{P_{H_2}}{C_{H_2}^{ref} H_{H_2}}\right)^{0.5} [e^{\alpha_a F \eta_a / RT} - e^{-\alpha_c F \eta_a / RT}]$	A m^{-3}
Electrochemical kinetics	$j_c = 4F \frac{P_{O_2}}{H_{O_2}} \left(\frac{1}{E_r k_c (1 - \epsilon_{CL})} + \frac{r_{agg} + \delta_i + \delta_w}{r_{agg}} \left(\frac{\delta_i}{a_{agg,i} D_{O_2,i}} + \frac{\delta_w}{a_{agg,w} D_{O_2,w}} \right) \right)^{-1}$	A m^{-3}
Over-potential	$\eta_a = \phi_s - \phi_m, \eta_c = \phi_s - \phi_m - V_{oc}$	V
Open circuit voltage	$V_{oc} = 1.229 - 8.456 \times 10^{-4}(T - 298.15) + 4.31 \times 10^{-5} T \ln(P_{H_2} P_{O_2}^{0.5})$	V
Active surface area	$a_{eff} = \frac{m_{pt}}{t_{CL}} (227.79 f^3 - 158.57 f^2 - 201.53 f + 159.5) \times 10^3$	m^{-1}
Proton conductivity	$\sigma_m = (0.514 \lambda - 0.326) e^{1268 \left(\frac{1}{303} - \frac{1}{T}\right)}$	S m^{-1}
Effective conductivity	$\sigma_{eff,s} = (1 - \epsilon_{GDL})^{1.5} \sigma_s, \sigma_{eff,m} = (1 - \epsilon_{CL} - L_i)^{1.5} \sigma_s$ $\sigma_{eff,m} = L_i^{1.5} \sigma_m$	S m^{-1}

Relative permeability	$K_{rl} = Ks^3, K_{rg} = K(1 - s)^3$	m^2
Capillary diffusivity	$D_s = -\frac{Ks^3 dP_c}{\mu_l ds}$	$\frac{m^2 s^{-1}}{1}$
Capillary pressure	$P_c = \sigma \cos(\theta) \left(\frac{\varepsilon}{K}\right)^{0.5} (1.417s - 2.12s^2 + 1.263s^3)$	Pa
Saturation pressure	$\log_{10} P_{sat} = -2.1794 + 0.02953(T - 273.15) - 9.1837 \times 10^{-5}(T - 273.15)^2 + 1.4454 \times 10^{-7}(T - 273.15)^3$	Pa
Electro-osmotic drag coefficient	$n_d = 2.5 \frac{\lambda}{22}$	-
Dissolved water diffusivity	D_λ	$\frac{m^2 s^{-1}}{1}$
Equilibrium water content	$\lambda^{eq} = \begin{cases} 1.41 + 11.3a - 18.8a^2 + 16.2a^3 & (a < 1) \\ 10.1 + 2.94(a - 1) & (a \geq 1) \end{cases}$	-
Water activity	$a = \frac{X_{wv}P}{P_{sat}} + 2s$	-
Oxygen diffusivity in liquid water	$D_{O_2,w} = 7.4 \times 10^{-12} \frac{T(\psi M_{H_2O})^{0.5}}{\mu_{H_2O} V_{O_2}^{0.6}}$	$\frac{m^2 s^{-1}}{1}$
Oxygen diffusivity in ionomer	$D_{O_2,i} = 2.88 \times 10^{-10} e^{[2933(\frac{1}{313} - \frac{1}{T})]}$	$\frac{m^2 s^{-1}}{1}$

Table 4. Source terms in the governing equations [14].

Description	Units
$S_{H_2} = -\frac{j_a}{2F} M_{H_2}$ Anode CL	$kg m^{-3} s^{-1}$
$S_{O_2} = -\frac{j_c}{4F} M_{O_2}$ Cathode CL	$kg m^{-3} s^{-1}$
$S_{wv} = -S_l - S_{vd} M_{H_2O}$ Anode and cathode CLs	$kg m^{-3} s^{-1}$
$S_{wv} = -S_l$ Anode and cathode GDLs	
$S_T = j_a \eta_a - \frac{T \Delta S_a}{2F} j_a + \sigma_{eff,m} \ \nabla \phi_m\ ^2 + \sigma_{eff,s} \ \nabla \phi_s\ ^2 + S_l \Delta h_{lg}$ Anode CL	$W m^{-3}$
$S_T = j_c \eta_c - \frac{T \Delta S_c}{4F} j_c + \sigma_{eff,m} \ \nabla \phi_m\ ^2 + \sigma_{eff,s} \ \nabla \phi_s\ ^2 + S_l \Delta h_{lg}$ Cathode CL	
$S_T = \sigma_{eff,m} \ \nabla \phi_m\ ^2$ membrane	
$S_T = \sigma_{eff,s} \ \nabla \phi_s\ ^2 + S_l \Delta h_{lg}$ Anode and cathode GDLs	
$S_s = -j_a$ Anode CL	$A m^{-3}$
$S_s = +j_c$ Cathode CL	
$S_m = +j_a$ Anode CL	$A m^{-3}$
$S_m = -j_c$ Cathode CL	

$$S_l = S_{phase} \text{ Anode and cathode GDLs and CLs} \quad \text{kg m}^{-3} \text{ s}^{-1}$$

$$S_{phase} = \begin{cases} \gamma_{cond} \frac{\varepsilon(1-s)}{RT} M_{H_2O} (P_{wv} - P_{sat}) & P_{wv} \geq P_{sat} \\ \gamma_{evap} \frac{\varepsilon s}{RT} M_{H_2O} (P_{wv} - P_{sat}) & P_{wv} < P_{sat} \end{cases} \quad \text{kg m}^{-3} \text{ s}^{-1}$$

$$S_d = S_{vd} \text{ Anode CL} \quad \text{mol m}^{-3} \text{ s}^{-1}$$

$$S_d = S_{vd} + S_\lambda \text{ Cathode CL}$$

$$S_{vd} = \gamma \frac{\rho_m}{M_m} (\lambda^{eq} - \lambda) \text{ Anode and cathode CLs}$$

$$S_\lambda = \frac{j_c}{2F} \text{ Cathode CL}$$

3. RESULTS AND DISCUSSION

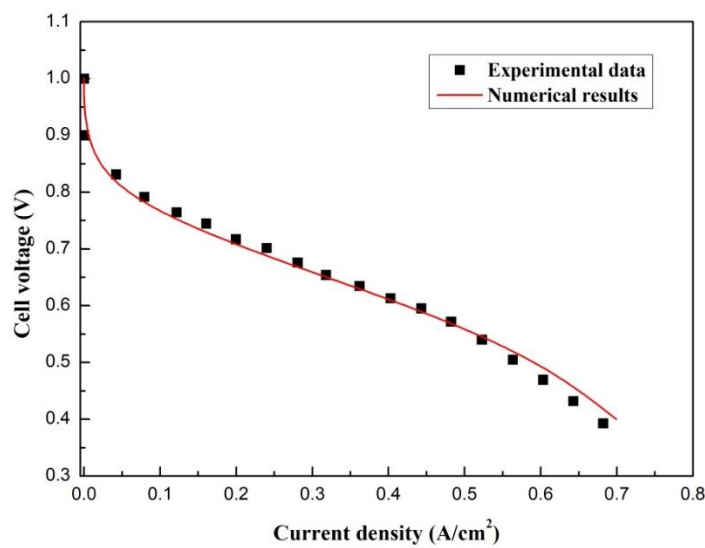


Figure 2. Comparison between the numerical results and experimental data.

As shown in Fig. 2, the polarization curve obtained by experimental measurements was compared with that predicted by the mathematical model. It can be seen that the numerical results show a good agreement with the experimental data reported by Yan et al. [20]. The experimental operating temperature is 353 K, and the operating pressure is 1.0 atm. Air and hydrogen were fully humidified and fed into the cathode and anode gas flow channels, respectively.

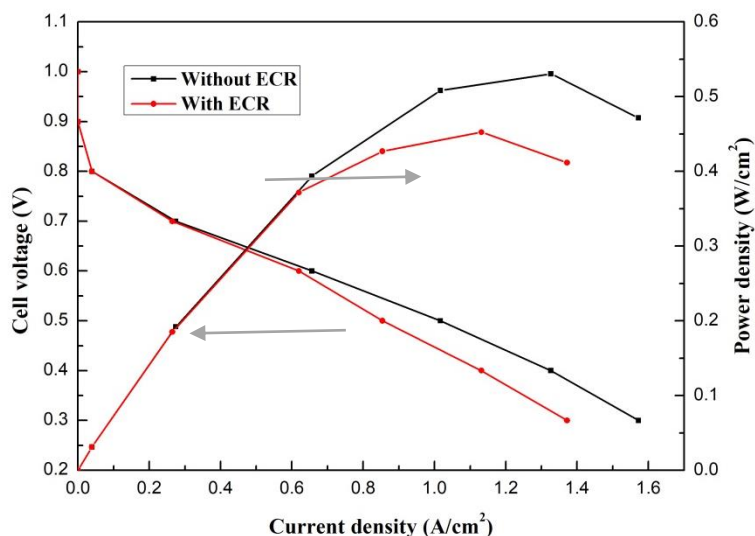


Figure 3. Cell performance of PEMFCs with/without electrical contact resistance (ECR).

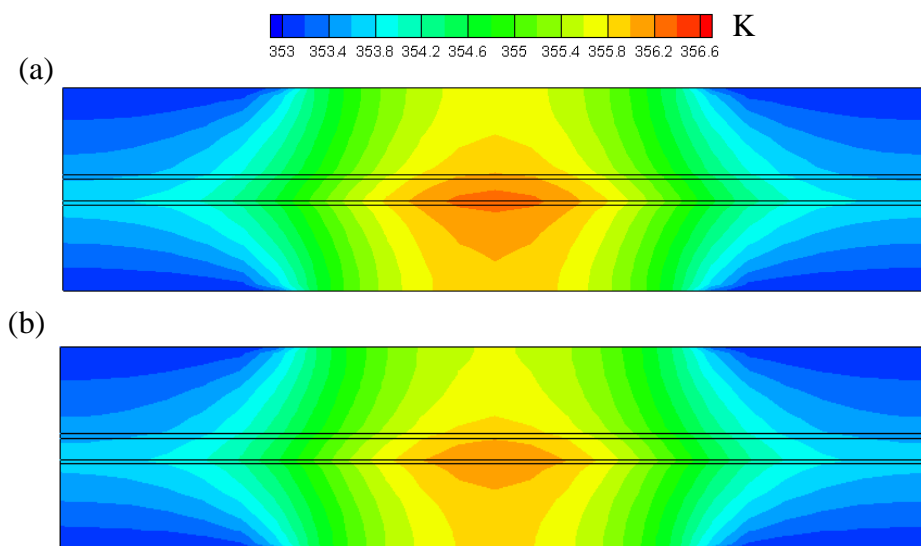


Figure 4. Temperature distributions of PEMFCs: (a) without electrical contact resistance (ECR) (b) with electrical contact resistance (ECR).

The electrical contact resistance (ECR) is quickly decreased and then reaches a constant value when the assembly force is gradually increased. In this study, the ECR of $9 \text{ m}\Omega \text{ cm}^2$ is applied [16]. The cell performance of PEMFCs with/without ECR is presented and compared, as shown in Fig.3. It is clearly seen that the cell performance predicted by the mathematical model with ECR is lower than that predicted by the mathematical model without ECR, especially at low cell voltages. At the cell voltage 0.6 V, the current densities of two cases are 0.656 A/cm^2 and 0.619 A/cm^2 , respectively. And the corresponding power densities are 0.394 W/cm^2 and 0.372 W/cm^2 , respectively.

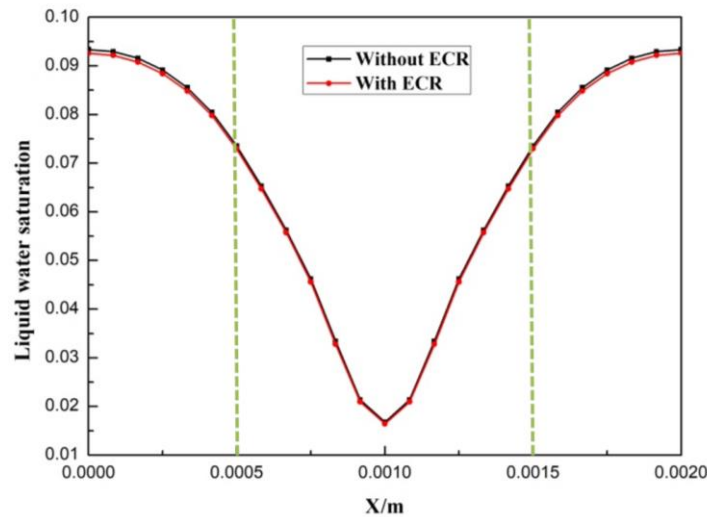


Figure 5. Liquid water saturation at the cathode GDL and CL interface of PEMFCs with/without electrical contact resistance (ECR).

Similar work was also carried out by Akbari et al [13]. However, the effect of liquid was not included in the mathematical model. In this study, a two-dimensional, non-isothermal and two-phase flow model was applied to investigate the effect of ECR on the cell performance and local transport phenomena of PEMFCs. In the following section, the temperature, liquid water saturation and solid phase potential of PEMFCs at the operating cell voltage 0.6 V are illustrated. Fig.4 shows the temperature distributions of two cases. It can be seen that the maximum temperature appears at the middle region of cathode CL, and minimum temperature appears at the regions close to the current collectors. And the maximum temperature is also decreased when the effect of ECR is included in the mathematical model.

The liquid water saturation at the GDL and CL interface of two cases are shown in Fig.5. It is clear that liquid water saturation at the regions under current collectors is greater than that at the region under the flow channel. This is mainly attributed to the temperature distributions. It can be seen that the liquid water saturation is only slightly affected at the regions under current collectors. The liquid water saturation level of the case without ECR is greater than that of the case with ECR.

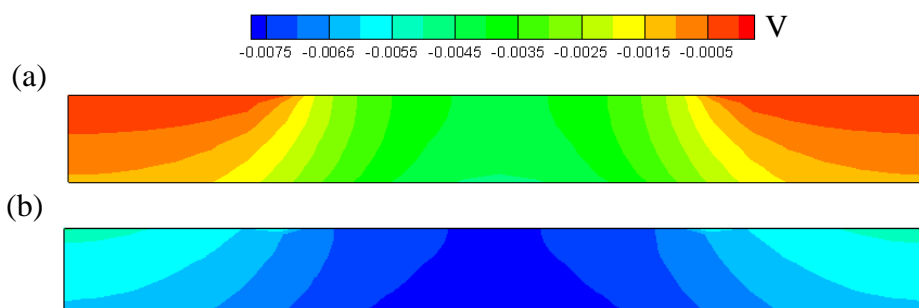


Figure 6. Solid phase potential distributions at the anode GDL of PEMFCs: (a) without electrical contact resistance (ECR) (b) with electrical contact resistance (ECR).

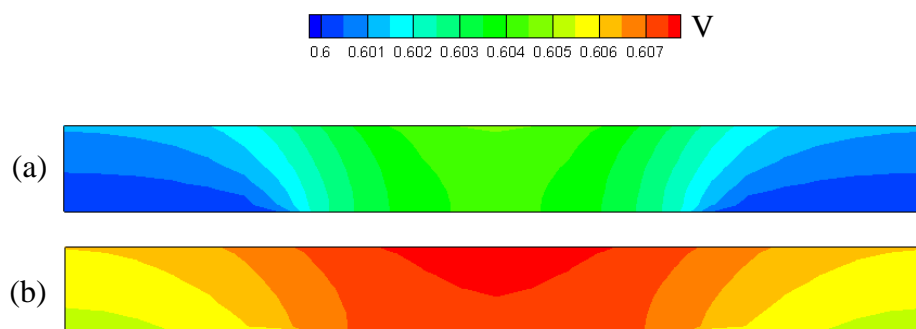


Figure 7. Solid phase potential distributions at the cathode GDL of PEMFCs: (a) without electrical contact resistance (ECR) (b) with electrical contact resistance (ECR).

Electrons generated at the anode CL are transferred to the cathode side through the electric load attached and then consumed at the cathode CL. The electron transport process is described by the Eq.3. The solid phase potential distributions at the anode and cathode GDLs are shown in Figs.6-7. It can be clearly seen that the solid phase potential increase from the bottom to the top at both the anode side and cathode side. Similar solid phase potential distributions were obtained by Meng and Wang [12]. In that study, the effect of electron transport through the GDL was systematically investigated. The solid phase potential profiles of Line-1 and Line-2 for two cases are plotted in Figs. 8-9. As shown in Fig.10, the solid phase potential of Line-1 is increased from -0.0013 V to 0 V, and that of Line-1 in increased from -0.0064V to -0.0056 V. As shown in Fig.11, the solid phase potential of Line-1 is increased from 0.6 V to 0.601 V, and that of Line-1 in increased from 0.605V to 0.605 V. This is attributed to the increased electrical transfer resistance between the GDLs and current collectors.

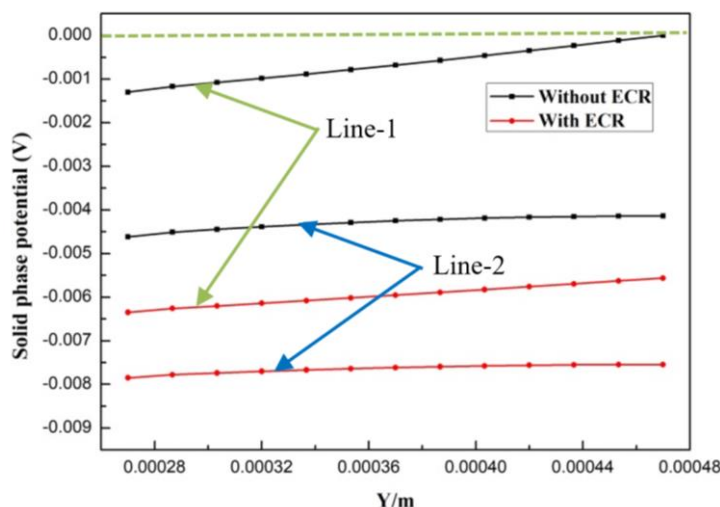


Figure 8. Solid phase potential distributions at the Line-1 and Line-2 of anode GDL.

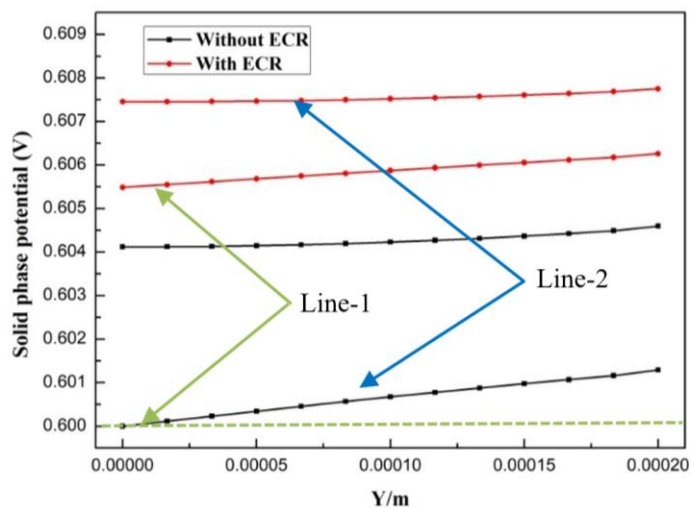


Figure 9. Solid phase potential distributions at the Line-1 and Line-2 of cathode GDL.

4. CONCLUSIONS

In this study, a two-dimensional, non-isothermal and two-phase flow model was applied to investigate the effect of electrical contact resistance on cell performance and transport characteristics of PEMFCs. The cell performance is significantly decreased when the contact resistance between the current collector and gas diffusion layer is applied in the mathematical model, especially at low cell voltages. The maximum temperature is decreased and the liquid water saturation is also slightly decreased when the electrical contact resistance is taken into account. The solid phase potential magnitude is also significantly affected by electrical contact resistance. It is strongly recommended that the effect of electrical contact resistance must be included in the mathematical model simulations.

ACKNOWLEDGMENTS

The authors gratefully acknowledge the financial supports from National Natural Science Foundation of China (No.51606013 and No.51779025). This work is also funded by the Fundamental Research Funds for the Central Universities of China (No.3132019191, No.3132019187 and No. 3132019327), China Postdoctoral Science Foundation (No.2019M651097 and No.2019M651094) and Natural Science Foundation of Liaoning Province (No.2019-BS-026 and No.2019-ZD-0154).

References

1. T.D. Tran, S. Huang, D.H. Vu, V.N. Duy, *Int. J. Electrochem. Sci.*, 13 (2018) 10480.
2. Q.W. Shen, L.N. Sun, B.W. Wang, *Int. J. Electrochem. Sci.*, 14 (2019) 1698.
3. Q.W. Shen, S.A. Li, G.G. Yang, N.B. Huang, *Int. J. Electrochem. Sci.*, 14 (2019) 5344.
4. Q.W. Shen, S.A. Li, G.G. Yang, N.B. Huang, J.L. Yuan, B. Sunden, *Numer. Heat Transf. A-Appl.*, 75 (2019) 509.
5. G. Hu, C. Ji, Y. Xia, Y. Suo, X. Wu, Z. Zhang, *Int. J. Electrochem. Sci.*, 14 (2019) 1358.
6. S.A. Li, B. Sunden, *Int. J. Hydrogen Energy*, 42 (2017) 27323.

7. S.A. Li, B. Sunden, *Int. J. Hydrogen Energy*, 43 (2018) 16279.
8. S. Shimpalee, S. Dutta, *Numer. Heat Transf. A-Appl.*, 38 (2000) 111.
9. Y. Wang, C. Y. Wang, *J. Electrochem. Soc.*, 153 (2006) A1193.
10. S.A. Li, B. Sunden, *Int. J. Numer. Methods Heat Fluid Flow*, 28 (2018) 1684.
11. S.A. Li, B. Sunden, *Numer. Heat Transf. A-Appl.*, 74 (2018) 917.
12. H. Meng, C.Y. Wang, *J. Electrochem. Soc.*, 151 (2004) A358.
13. M.H. Akbari, B. Rismanchi, *Renew. Energy*, 33 (2008) 1775.
14. V. Mishra, F. Yang, R. Pitchumani, *ASME J. Fuel Cell Sci. Technol.*, 1 (2004) 2.
15. H. Wang, M.A. Sweikart, J.A. Turner, *J. Power Sources*, 115 (2003) 243.
16. A. Vikram, P.R. Chowdhury, R.K. Phillips, M. Hoorfar, *J. Power Sources*, 320 (2016) 274.
17. S.A. Li, J.L. Yuan, G.N.Xie, B. Sunden, *Int. J. Hydrogen Energy*, 43 (2018) 8451.
18. H. Meng, *J. Power Sources*, 168 (2007) 218.
19. T.F. Cao, Y.T. Mu, J. Ding, H. Lin, Y.L. He, W.Q. Tao, *Int. J. Heat Mass Transf.*, 87 (2015) 544.
20. Q.G. Yan, H. Toghiani, H. Causey, *J. Power Sources*, 161 (2006) 492.

© 2019 The Authors. Published by ESG (www.electrochemsci.org). This article is an open access article distributed under the terms and conditions of the Creative Commons Attribution license (<http://creativecommons.org/licenses/by/4.0/>).